PHYSICAL REVIEW LETTERS **122,** 155001 (2019)

Picosecond Thermodynamics in Underdense Plasmas Measured with Thomson Scattering

A. S. Davies,[1,2*] D. Haberberger,[1] J. Katz,[1] S. Bucht,[1,2] J. P. Palastro,[1] W. Rozmus,[3,4] and D. H. Froula[1,2]
[1]*Laboratory for Laser Energetics, University of Rochester, 250 E River Road, Rochester, New York 14623, USA*
[2]*Department of Physics and Astronomy, University of Rochester, Rochester, New York 14623, USA*
[3]*Theoretical Physics Institute, Department of Physics, University of Alberta, Edmonton, Alberta, Canada T6G 2E1*
[4]*High Energy Density Science Division, SLAC National Accelerator Laboratory, Menlo Park, California 94025, USA*

(Received 30 October 2018; revised manuscript received 14 January 2019; published 15 April 2019)

The rapid evolutions of the electron density and temperature in a laser-produced plasma were measured using collective Thomson scattering. Unprecedented picosecond time resolution, enabled by a pulse-front-tilt compensated spectrometer, revealed a transition in the plasma-wave dynamics from an initially cold, collisional state to a quasistationary, collisionless state. The Thomson-scattering spectra were compared with theoretical calculations of the fluctuation spectrum using either a conventional Bhatnagar-Gross-Krook (BGK) collision operator or the rigorous Landau collision terms: the BGK model overestimates the electron temperature by 50% in the most-collisional conditions.

DOI: 10.1103/PhysRevLett.122.155001

Endeavors to engineer plasmas for a number of applications rely critically on plasma conditions. Optimizing plasma devices, including laser amplifiers [1–3], laser compressors [4], wave plates [5,6], polarizers [7,8], Q plates [9], particle accelerators [10,11], photon accelerators [12], high-order frequency conversion [13,14], and photon-electron light sources [15,16], requires an accurate knowledge of plasma density and temperature dynamics. In these systems, the electromagnetic fields generate dynamic plasma conditions that typically evolve over the initial 50 ps. During the rise of a high-intensity laser pulse, the photoionized electrons are liberated with minimal kinetic energy, resulting in an initially cold plasma. The energy supplied to the electrons by the electromagnetic field through inverse bremsstrahlung causes the temperature to rise rapidly until the collisionality of the plasma reduces the heating rate to a level comparable to the cooling mechanisms. Measurements of these early plasma dynamics on application-relevant timescales have been previously unattainable.

Optical Thomson scattering (TS) is a powerful diagnostic that can accurately measure plasma conditions [17–23], but it has had limited temporal resolution (>50 ps) [24]. Experiments have used ultrashort (<1 ps) TS probe beams [20,25] to improve the temporal resolution, but these studies were limited to conditions where the width of the scattered features were large as compared to the bandwidth associated with time integrating the scattered light from an ultrashort probe beam. Furthermore, during plasma formation, the collisional damping dominates over the Landau damping of electron plasma waves (EPWs) and a collisional theory is required to accurately model the TS spectrum. Thomson-scattering measurements of collisional EPWs have been limited to nonideal plasmas, $\Lambda = 4 \times 10^8 T_e^{3/2}(\mathrm{eV})/n_e^{1/2}\ (\mathrm{cm}^3) \lesssim 1$, where there are few particles in the Debye sphere and the short-range Coulombic interaction between charges determines the dynamics, as opposed to the collective behavior [26–29]. In these nonideal plasmas, theories have been developed to interpret the TS spectrum [30,31]. The standard computationally efficient approach to include collisions is to use the approximate Bhatnagar-Gross-Krook (BGK) collision operator [32,33]; but, recently, the more-accurate linearized Vlasov-Fokker-Planck (VFP) equation was presented to account for collisions in TS calculations [34].

In this Letter, we report the first observation of the effects of collisions on electron plasma waves in the transition to an ideal plasma. The measurements were obtained by an ultrafast high-throughput spectrometer that provided unprecedented temporal resolution of the EPW TS spectra. These spectra provided a measurement of collisional EPWs that were modeled to extract the picosecond evolution of the electron temperature and density. The standard treatment of an ideal plasma is to assume that Landau damping is the only active damping mechanism; however, the measurements of the initial plasma demonstrated that the EPW damping was dominated by collisions. The hydrogen gas was ionized at an intensity near $10^{14}\ \mathrm{W/cm}^2$, where the initial electron plasma temperature and density were measured to be 3 eV and $8.40 \times 10^{18}\ \mathrm{cm}^3$, respectively. Over the first 18 ps, the plasma temperature increased modestly (16 eV) as the plasma density became fully ionized ($1.07 \times 10^{19}\ \mathrm{cm}^3$) and then rapidly increased to a saturated level of 93 eV over the next 20 ps. During this evolution, the plasma transitioned from a nonideal ($\Lambda \sim 1$) to an ideal ($\Lambda \sim 110$) plasma. For temperatures below 45 eV, a collisional model was required to reproduce the measured spectrum. For the most-collisional conditions, the VFP scattering model shows that the BGK model significantly overestimates the effects of collisions, leading to an overestimation of the electron temperature by 50%.

The experiments were conducted on the Multi-Terawatt Laser facility [35] at the University of Rochester's Laboratory for Laser Energetics. The 1054-nm-pump laser irradiated a 4-mm-long hydrogen gas cell [Fig. 1(a)] at a molecular density of $\sim 5 \times 10^{18}$ cm^{-3} with a chirped 60 ps full-width-at-half-maximum (FWHM) square pulse (~5 ps rise time). A fraction of the pump beam was frequency doubled (500 mJ) and co-propagated along with the remaining 1.4 J of pump energy. The beams were focused in an $f/25$ cone by a spherical mirror to an elliptical spot [Fig. 1(b)]. The 160×50 μm (FWHM) pump beam spot generated a peak vacuum intensity of $\sim 2.5 \times 10^{14}$ W/cm^2. The focal spot size of the probe beam was about half the size of the pump beam. Due to the copropagation of the pump and probe along with achromatic focusing, the two beams were perfectly concentric in the focal volume. The bandwidth of the probe beam (~2 nm) was spread linearly in time over the pulse duration. This resulted in an effective bandwidth over the diagnostics temporal resolution of ~0.07 nm. To identify ionization thresholds using an interferometer, a low energy 60 ps 2ω probe beam was propagated through the gas cell perpendicular to the main beams.

The $\lambda = 526.5$ nm light, scattered from a $60 \times 60 \times 30$ μm volume at the center of the gas cell, was collected and collimated by an $f/2.4$ achromatic lens located 90° from the laser beam's propagation axis. The collected light was focused with an $f/4$ achromatic lens onto a 0.1-mm-diameter aperture at the entrance of an $f/3$ pulse-front-tilt compensated spectrometer that was coupled to an ultrafast optical streak camera (ROSS P820) [36]. The spectrometer collimated the light in a 100-mm-diameter beam that was reflected from an echelon before propagating through a transmission grating and focused onto the streak camera slit. An ~200-μm-wide neutral density filter was positioned at the streak-camera slit to reduce light scattered around the probe wavelength. The finite focusing and collection optics were included in the calculated spectra.

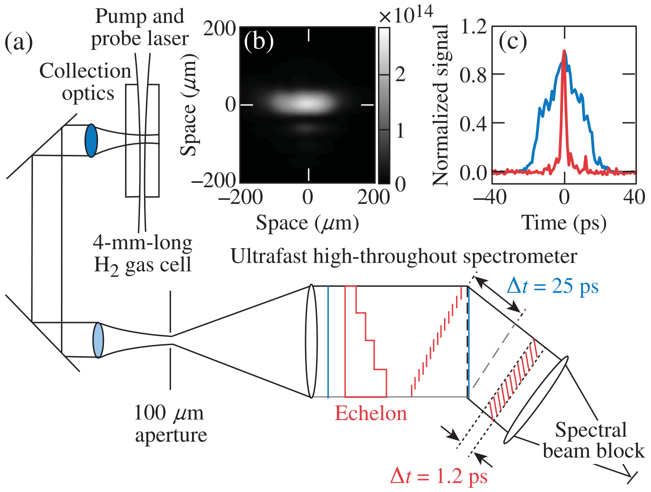

FIG. 1. (a) A schematic of the setup that shows the spectrometers pulse-front tilt with (red lines, $\Delta t = 1.2$ ps) and without (blue lines, $\Delta t = 25$ ps) the echelon installed. For schematic purposes, a transmission echelon is shown. (b) The 1ω beam focal spot. (c) The measured temporal response function with (red line) and without (blue line) the echelon installed.

The spectral instrument resolution function (IRF) in this system (1.23 nm FWHM) was dominated by the diameter of the aperture at the entrance of the spectrometer, but it included estimates from broadening by spatial gradients (~0.15 nm), finite collection optics (~0.06 nm), and the instantaneous bandwidth of the probe beam (~0.07 nm). For further details, see the Supplemental Material SM [37]. To achieve the necessary spectral resolution for the measurements, a linear grating density of 300 grooves/mm along with the 225-mm-focal-length spectrometer were used to spread the complete ~200 nm TS spectrum across the detector. The combination of the beam diameter and the grating density resulted in a total number of grooves illuminated of $N = 1.4 \times 10^4$.

The pulse-front-tilt compensated spectrometer was invented to trade unutilized resolving power ($\lambda/\Delta\lambda = N$, $\Delta\lambda \simeq 0.04$ nm) with temporal resolution ($\Delta t \sim N\lambda/c = 25$ ps) by using an echelon to separate the beam into $n = 20$ temporally delayed co-aligned beamlets. This reduced the pulse-front tilt of a conventional spectrometer with a streak-camera limited spectral resolution of $\Delta\lambda = 1$ nm from ~25 ps to $\Delta t_c = \Delta t/n \sim 1.25$ ps (see Fig. 1) while maintaining 1 nm spectral resolution. The resulting temporal and spectral resolutions were near the uncertainty principle limit ($\Delta t_{\text{limit}} = \lambda^2/\Delta\lambda c \simeq 0.9$ ps). By designing the spectrometer to correct for the 25 ps impulse response, the temporal resolution was improved by more than an order of magnitude. This can be seen in Fig. 1(c), which compares measurements of the spectrometer streak-camera system resolution obtained with and without the echelon installed. The temporal resolution $[G(t) = \exp(-4\ln(2)t^2/\tau^2)]$ of the system was measured as a function of photoelectrons to account for space-charge broadening in the streak camera during the data analysis ($\tau = 2$ to 5 ps over the entire data range).

Figure 2 shows that the wavelength separation between the blue and redshifted spectral peaks initially increases. This is a result of the increasing density and temperature: the wavelength separation between the features is proportional to the Langmuir frequency ($\sim\sqrt{\omega_{pe}^2 + 3v_{\text{th}}^2 k^2}$, where ω_{pe} is the plasma frequency and v_{th} is the electron thermal velocity). Late in time, this separation is relatively constant, indicating that the plasma is approaching steady state. The streaked spectrometer integrated the scattered spectrum over the temporal instrument function ($\tau = 2$ ps); this was included in the spectrum calculations [Fig. 2(b)].

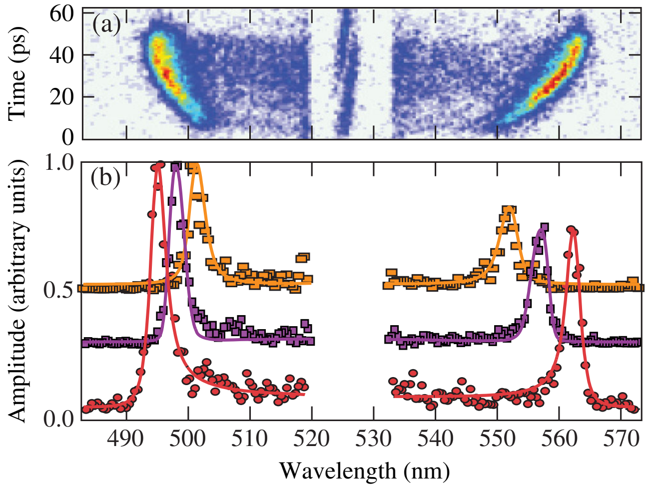

FIG. 2. (a) The TS spectrum shows the temporal evolution of the EPW features. Time zero coincides with the photoionization threshold laser intensity $\sim 10^{14}$ W/cm^2 of the pump beam. (b) The spectra at 9 ps (orange squares), 21 ps (purple squares), and 50 ps (red circles) were fit ($T_e^{9\text{ ps}} = 5$ eV, $n_e^{9\text{ ps}} = 8.9 \times 10^{18}$ cm^3, $T_e^{21\text{ ps}} = 26$ eV, $n_e^{21\text{ ps}} = 1.08 \times 10^{19}$ cm^3, $T_e^{50\text{ ps}} = 92$ eV, and $n_e^{50\text{ ps}} = 1.09 \times 10^{19}$ cm^3) with a scattering function that includes collisional effects through the BGK model (solid curves). The two peaks in the scattered spectrum were normalized to match the calculated spectrum's amplitude.

Figure 3 shows a summary of the picosecond plasma dynamics. The plasma was measured to initiate at a temperature of 3 eV and a density of 8.4×10^{18} cm^3. From this initial state, the plasma evolved to a steady-state temperature of 93 eV and a density of 1.07×10^{19} cm^3 over 40 ps. The plasma was calculated to be photoionized at an intensity near 10^{14} W/cm^2, which corresponded to about half of the peak intensity and occurred during the first few picoseconds of the rising laser pulse. This photoionized intensity threshold was confirmed by observing the onset of the interferometry and TS signals. During the first 13 ps, the plasma temperature was moderated by the energy required to dissociate (4.52 eV) and ionize (13.6 eV) hydrogen while also overcoming the cooling mechanisms of collisional excitation and ionization. Once the hydrogen was fully ionized, the plasma was heated by inverse bremsstrahlung absorption until an equilibrium (see Fig. 3) was reached with the thermal conduction to the surrounding gas.

Figure 2(b) shows that the measured and simulated spectra are in excellent agreement. The temporal evolution was included in the calculated spectra by averaging the spectrum over the temporal instrument function,

$$P(t) = \sum_{t-\tau/2}^{t+\tau/2} G_i(t) P_i(\boldsymbol{k}, \omega),$$

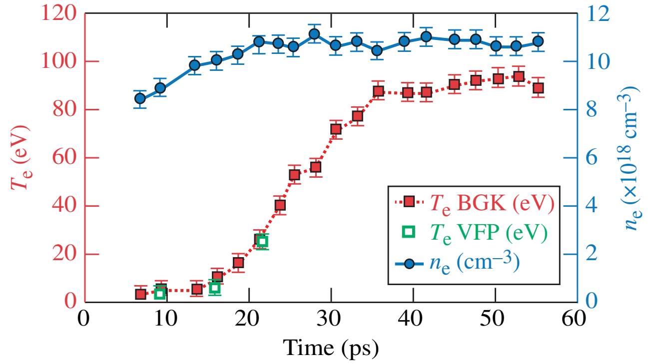

FIG. 3. The measured electron temperature (red squares, left axis) and density (blue circles, right axis), determined using the computationally efficient BGK approximation to calculate the spectrum, show the rapid evolution of the plasma. The parameters determined by the VFP collisional model are shown (green open squares). The densities determined with the VFP model were identical to the densities (blue circles) determined when using the BGK model.

where $P_i(\boldsymbol{k}, \omega)$ is the scattered power calculated with the plasma conditions at each time [38]. The TS spectra were initially fit to determine the electron temperature and density late in time ($t = 50$ ps) when there was no temporal evolution [Fig. 2(b)]. The evolution of the plasma conditions was then determined by iteration. In the first iteration, the temperature evolution was calculated by assuming a constant density, which was found using the late time fit ($t = 50$ ps). In all following iterations, both the temperature and density evolutions from the previous iteration were used. The process was repeated until the plasma conditions between subsequent iterations remained unchanged, which was achieved in the third iteration.

The spectra were calculated from the spectral density function [38],

$$P(\boldsymbol{k}, \omega) = -\frac{A}{\omega}\left(1 + \frac{2\omega}{\omega_0}\right) \mathrm{Im}\left(\frac{g(\boldsymbol{k}, \omega)}{\epsilon(\boldsymbol{k}, \omega)}\right), \qquad (1)$$

where A is a normalization constant. For the most-collisional conditions ($T_e < 18$ eV), a high-frequency (HF) approximation to the VFP dynamic structure factor [cf. Eqs. (55)–(57) from [34]] was used, where $g(\boldsymbol{k}, \omega) = (J_N^N - \chi_e^{\mathrm{HF}})$, $\epsilon^{\mathrm{HF}}(\boldsymbol{k}, \omega) = 1 + \chi_e^{\mathrm{HF}} = 1 + [(1 + i\omega J_N^N)/k^2\lambda_D^2]$ is the plasma dielectric function [39], J_N^N is the velocity moment of the zero-order harmonic from the solution to the complete VFP equations [34,39], $\omega = \omega_0 - \omega_s$ is the plasma-wave frequency, $\boldsymbol{k} = \boldsymbol{k}_0 - \boldsymbol{k}_s$ is the electron plasma-wave vector, $\boldsymbol{k}_0$ is the TS probe wave vector, $\boldsymbol{k}_s$ is the TS light wave vector, ω_0 is the TS probe frequency, ω_s is the TS light frequency, and λ_D is the Debye length.

Figure 4 shows that the TS spectrum calculated with the VFP model is an excellent fit to the measured spectrum. At these conditions, using the collisionless model results in a

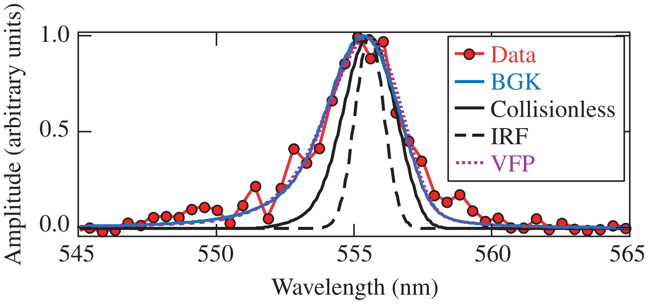

FIG. 4. The measure spectrum (red circles) at 16 ps is compared to calculations that use a collisionless model (black solid curve: $T_e = 10$ eV and $n_e = 1.0 \times 10^{19}$ cm^3), a VFP model (purple dashed curve: $T_e = 5$ eV and $n_e = 1.0 \times 10^{19}$ cm^3), and a BGK model (blue curve: $T_e = 10$ eV and $n_e = 1.0 \times 10^{19}$ cm^3). The spectra were calculated with the plasma conditions over the surrounding 2 ps and convolved with the IRF (black dashed curve).

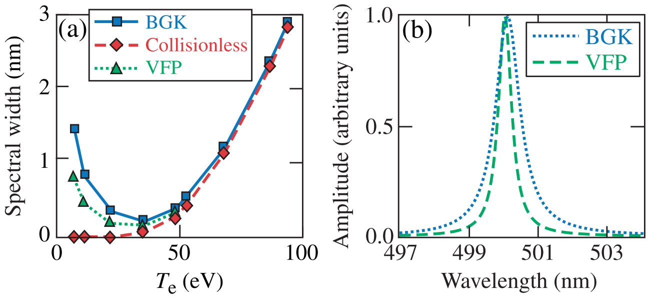

FIG. 5. (a) The width (FWHM) of the redshifted EPW features is plotted for a density of 10^{19} cm^3 using the collisionless (red diamonds), BGK (blue squares), and VFP (green triangles) models as functions of electron temperature. (b) The spectrum calculated with the BGK model (blue dashed line) and the VFP model (green dashed line) are shown for $T_e = 11$ eV and $n_e = 1.07 \times 10^{19}$ cm^3. To illustrated the width differences, the BGK spectrum was multiplied by 1.8.

spectrum that was essentially a delta function, and the experimental width was dominated by the temporal evolution in density and the instrument response function, which were narrower than the measurements. The TS spectra calculated with the BGK collisional model reproduced the measured scattering spectrum at all times; but, in the most-collisional conditions, it overestimated the electron temperature by ~50% [Fig. 3]. Detailed studies [33] that have compared the BGK model to more complete theories based on the VFP kinetic equations have concluded that neglecting the electron-electron collisions and the crude approximation to the Coulomb collision operator in the BGK model leads to significant differences in the plasma response at Langmuir fluctuation frequencies [39,40]. This leads to inaccurate calculations of the temperature when using the BGK model.

The TS spectrum calculated with the BGK model [34,38] used Eq. (1), where $g^{\mathrm{BGK}}(\boldsymbol{k},\omega) = -k^2\lambda_D^2$ and the plasma dielectric function follows from the BGK model [32,33]:

$$\epsilon^{\mathrm{BGK}}(\boldsymbol{k},\omega) = 1 + \frac{4\pi e^2}{m_e k^2}\int d^3v \frac{1}{\omega + i\nu_{\mathrm{ei}}(v) - \boldsymbol{k}\cdot\boldsymbol{v}}\boldsymbol{k}\cdot\frac{\partial F_e}{\partial \boldsymbol{v}}. \tag{2}$$

Here, the electron-ion collision frequency is given by $\nu_{ei} = 4\pi Z e^4 n_e \Lambda_{\mathrm{ei}}/m_e^2 v^3$, $F_e = n_e(m_e/2\pi T_e)^{3/2}$ exp $(-m_e v^2/2T_e)$ is the electron's Maxwellian velocity distribution, v is electron velocity, m_e is the electron mass, e is the electron charge, and n_e and T_e are the electron density and temperature, respectively. The BGK model is often simplified by using the thermal velocity in the collisional term ν_{ei}, but to improve its accuracy in these calculations, the velocity dependence was retained [38]. The standard collisionless results for the TS spectrum [Eq. (1)] are recovered in the limit of $\nu_{\mathrm{ei}} = 0$ [38].

Figure 5 shows the spectral width of the EPW features, which is proportional to the EPW damping, for the collisionless, BGK, and VFP models. At a density of 10^{19} cm^3, a damping minimum is obtained at 35 eV for both the VFP and BGK models. This minimum in damping is a result of the competition between the collisional damping that dominates at low temperatures and the collisionless (Landau) damping that dominates at high temperatures. The collisionless model works well for temperatures above >35 eV. Collisional damping is important in calculating the width at temperatures below ~35 eV. This is consistent with the measurements, which indicated that a collisional theory was required to accurately interpret the spectra at these temperatures. Figure 5(b) compares the spectra calculated using the BGK and the VFP models, but without measurement effects. The BGK model is a good approximation for determining the resonant frequency, but it overestimates the width of the spectrum when collisions are important ($T_e \lesssim 35$ eV). This results in an overestimate of the electron temperature. The deviations from the VFP model reveal when improved theoretical interpretations of TS experiments are required.

In summary, limiting the pulse-front tilt in a spectrometer has allowed an ultrafast TS diagnostic to measure the plasma creation and picosecond evolution of the electron temperature and density in a laser-produced plasma. The measurements were compared with spectra calculated using the standard BGK model to account for collisions and show that the BGK model overestimates the spectral width of the EPW features, leading to an overestimate of the electron temperature by up to ~50% at the most-collisional conditions. This overestimation of collisions by the BGK model has implications that extend well beyond TS because this collisional model is often used in plasma physics, including modeling of thermal transport.

These picosecond electron temperature and density measurements can be applied to laser-plasma devices that require knowledge of the rapidly evolving plasma conditions. Laser-plasma Raman amplifiers require frequency matching between an electromagnetic beat wave and the plasma frequency for efficient energy transfer from a pump laser to the seed [4]; but, if the plasma frequency is rapidly evolving, as these experiments show, the amplifier will be detuned and the efficiency will be poor [41–45]. With measurements of the plasma evolution, the system could be properly tuned to recover efficient energy transfer.

The work published here was supported by the U.S. Department of Energy Office of Fusion Energy Sciences under Contract No. DE-SC0016253, the U.S. Department of Energy under Cooperative Agreement No. DE-NA0003856, the University of Rochester, the New York State Energy Research and Development Authority, and the DOE Fusion Energy Sciences user Contract No. FWP100182. This Letter was prepared as an account of work sponsored by an agency of the U.S. Government. Neither the U.S. Government nor any agency thereof, nor any of their employees, makes any warranty, express or implied, or assumes any legal liability or responsibility for the accuracy, completeness, or usefulness of any information, apparatus, product, or process disclosed, or represents that its use would not infringe privately owned rights. Reference herein to any specific commercial product, process, or service by trade name, trademark, manufacturer, or otherwise does not necessarily constitute or imply its endorsement, recommendation, or favoring by the U.S. Government or any agency thereof. The views and opinions of authors expressed herein do not necessarily state or reflect those of the U.S. Government or any agency thereof.

---

[*] adavies@lle.rochester.edu

[1] Y. Ping, W. Cheng, S. Suckewer, D. S. Clark, and N. J. Fisch, Phys. Rev. Lett. **92**, 175007 (2004).

[2] J. Ren, W. Cheng, S. Li, and S. Suckewer, Nat. Phys. **3**, 732 (2007).

[3] G. Vieux, S. Cipiccia, D. W. Grant, N. Lemos, P. Grant, C. Ciocarlan, B. Ersfeld, M. S. Hur, P. Lepipas, G. G. Manahan *et al.*, Sci. Rep. **7**, 2399 (2017).

[4] V. M. Malkin, G. Shvets, and N. J. Fisch, Phys. Rev. Lett. **82**, 4448 (1999).

[5] P. Michel, L. Divol, D. Turnbull, and J. D. Moody, Phys. Rev. Lett. **113**, 205001 (2014).

[6] D. Turnbull, P. Michel, T. Chapman, E. Tubman, B. B. Pollock, C. Y. Chen, C. Goyon, J. S. Ross, L. Divol, N. Woolsey *et al.*, Phys. Rev. Lett. **116**, 205001 (2016).

[7] D. J. Stark, C. Bhattacharjee, A. V. Arefiev, T. Toncian, R. D. Hazeltine, and S. M. Mahajan, Phys. Rev. Lett. **115**, 025002 (2015).

[8] D. Turnbull, C. Goyon, G. E. Kemp, B. B. Pollock, D. Mariscal, L. Divol, J. S. Ross, S. Patankar, J. D. Moody, and P. Michel, Phys. Rev. Lett. **118**, 015001 (2017).

[9] K. Qu, Q. Jia, and N. J. Fisch, Phys. Rev. E **96**, 053207 (2017).

[10] R. Bingham, Nature (London) **394**, 617 (1998).

[11] S. M. Hooker, Nat. Photonics **7**, 775 (2013).

[12] S. C. Wilks, J. M. Dawson, and W. B. Mori, Phys. Rev. Lett. **61**, 337 (1988).

[13] J. J. Rocca, V. Shlyaptsev, F. G. Tomasel, O. D. Cortazar, D. Hartshorn, and J. L. A. Chilla, Phys. Rev. Lett. **73**, 2192 (1994).

[14] A. Butler, A. J. Gonsalves, C. M. McKenna, D. J. Spence, S. M. Hooker, S. Sebban, T. Mocek, I. Bettaibi, and B. Cros, Phys. Rev. Lett. **91**, 205001 (2003).

[15] K. T. Phuoc, S. Corde, C. Thaury, V. Malka, A. Tafzi, J.-P. Goddet, R. C. Shah, S. Sebban, and A. Rousse, Nat. Photonics **6**, 308 (2012).

[16] N. D. Powers, I. Ghebregziabher, G. Golovin, C. Liu, S. Chen, S. Banerjee, J. Zhang, and D. P. Umstadter, Nat. Photonics **8**, 28 (2014).

[17] S. H. Glenzer, W. Rozmus, B. J. MacGowan, K. G. Estabrook, J. D. De Groot, G. B. Zimmerman, H. A. Baldis, J. A. Harte, R. W. Lee, E. A. Williams *et al.*, Phys. Rev. Lett. **82**, 97 (1999).

[18] D. S. Montgomery, R. P. Johnson, J. A. Cobble, J. C. FernNdez, E. L. Lindman, H. A. Rose, and K. G. Estabrook, Laser Part. Beams **17**, 349 (1999).

[19] J. L. Kline, D. S. Montgomery, B. Bezzerides, J. A. Cobble, D. F. DuBois, R. P. Johnson, H. A. Rose, L. Yin, and H. X. Vu, Phys. Rev. Lett. **94**, 175003 (2005).

[20] C. Rousseaux, L. Gremillet, M. Casanova, P. Loiseau, M. R. Le Gloahec, S. D. Baton, F. Amiranoff, J. C. Adam, and A. Heron, Phys. Rev. Lett. **97**, 015001 (2006).

[21] D. H. Froula, L. Divol, A. A. Offenberger, N. Meezan, T. Ao, G. Gregori, C. Niemann, D. Price, C. A. Smith, and S. H. Glenzer, Phys. Rev. Lett. **93**, 035001 (2004).

[22] J. S. Ross, S. H. Glenzer, J. P. Palastro, B. B. Pollock, D. Price, G. R. Tynan, and D. H. Froula, Rev. Sci. Instrum. **81**, 10D523 (2010).

[23] R. J. Henchen, M. Sherlock, W. Rozmus, J. Katz, D. Cao, J. P. Palastro, and D. H. Froula, Phys. Rev. Lett. **121**, 125001 (2018).

[24] A. Visco, R. P. Drake, D. H. Froula, S. H. Glenzer, and B. B. Pollock, Rev. Sci. Instrum. **79**, 10F545 (2008).

[25] T. E. Glover, T. D. Donnelly, E. A. Lipman, A. Sullivan, and R. W. Falcone, Phys. Rev. Lett. **73**, 78 (1994).

[26] D. R. Nicholson, *Introduction to Plasma Theory* (Wiley, New York, 1983).

[27] S. C. Snyder, D. M. Crawford, and J. R. Fincke, Phys. Rev. E **61**, 1920 (2000).

[28] G. Gregori, U. Kortshagen, J. Heberlein, and E. Pfender, Phys. Rev. E **65**, 046411 (2002).

[29] B. B. L. Witte, L. B. Fletcher, E. Galtier, E. Gamboa, H. J. Lee, U. Zastrau, R. Redmer, S. H. Glenzer, and P. Sperling, Phys. Rev. Lett. **118**, 225001 (2017).

[30] W. Rozmus, S. H. Glenzer, K. G. Estabrook, H. A. Baldis, and B. J. MacGowan, Astrophys. J. Suppl. Ser. **127**, 459 (2000).

[31] G. Gregori and D. O. Gericke, Phys. Plasmas **16**, 056306 (2009).

[32] P. L. Bhatnagar, E. P. Gross, and M. Krook, Phys. Rev. **94**, 511 (1954).

[33] M. Opher, G. J. Morales, and J. N. Leboeuf, Phys. Rev. E **66**, 016407 (2002).

[34] W. Rozmus, A. Brantov, C. Fortmann-Grote, V. Y. Bychenkov, and S. Glenzer, Phys. Rev. E **96**, 043207 (2017).

[35] V. Bagnoud, I. A. Begishev, M. J. Guardalben, J. Puth, and J. D. Zuegel, Opt. Lett. **30**, 1843 (2005).

[36] J. Katz, R. Boni, R. Rivlis, C. Muir, and D. H. Froula, Rev. Sci. Instrum. **87**, 11E535 (2016).

[37] See Supplemental Material at http://link.aps.org/supplemental/10.1103/PhysRevLett.122.155001 for instrument response function details.

[38] J. Sheffield, D. H. Froula, S. H. Glenzer, and N. C. Luhmann, *Plasma Scattering of Electromagnetic Radiation: Theory and Measurement Techniques* (Elsevier Science, New York, 2010).

[39] A. V. Brantov, V. Y. Bychenkov, and W. Rozmus, Phys. Rev. Lett. **108**, 205001 (2012).

[40] V. Y. Bychenkov, Plasma Phys. Rep. **24**, 801 (1998).

[41] D. S. Clark and N. J. Fisch, Phys. Plasmas **10**, 3363 (2003).

[42] R. L. Berger, D. S. Clark, A. A. Solodov, E. J. Valeo, and N. J. Fisch, Phys. Plasmas **11**, 1931 (2004).

[43] J. P. Farmer, B. Ersfeld, and D. A. Jaroszynski, Phys. Plasmas **17**, 113301 (2010).

[44] N. A. Yampolsky and N. J. Fisch, Phys. Plasmas **18**, 056711 (2011).

[45] X. Yang, G. Vieux, E. Brunetti, B. Ersfeld, J. P. Farmer, M. S. Hur, R. C. Issac, G. Raj, S. M. Wiggins, G. H. Welsh *et al.*, Sci. Rep. **5**, 13333 (2015).